

Crossover of Ising- to Rashba-Type Superconductivity in Epitaxial $\text{Bi}_2\text{Se}_3/\text{Monolayer NbSe}_2$ Heterostructures

Hemian Yi^{1,7}, Lun-Hui Hu^{1,7}, Yuanxi Wang^{1,2,7}, Run Xiao¹, Jiaqi Cai³, Danielle Reifsnyder Hickey^{4,5}, Chengye Dong⁵, Yi-Fan Zhao¹, Ling-Jie Zhou¹, Ruoxi Zhang¹, Anthony R. Richardella¹, Nasim Alem⁵, Joshua A. Robinson⁵, Moses H. W. Chan¹, Xiaodong Xu^{3,6}, Nitin Samarth¹, Chao-Xing Liu¹, and Cui-Zu Chang¹

¹Department of Physics, The Pennsylvania State University, University Park, PA 16802, USA

²Department of Physics, University of North Texas, Denton, TX 76203, USA

³Department of Physics, University of Washington, Seattle, WA 98195, USA

⁴Department of Chemistry, The Pennsylvania State University, University Park, PA 16802, USA

⁵Department of Materials Science and Engineering, The Pennsylvania State University, University Park, PA 16802, USA

⁶Department of Materials Science and Engineering, University of Washington, Seattle, WA 98195, USA

⁷These authors contributed equally: Hemian Yi, Lun-Hui Hu, Yuanxi Wang

Corresponding author: cxc955@psu.edu (C.-Z. C.)

Abstract: A topological insulator (TI) interfaced with an *s*-wave superconductor has been predicted to host an unusual form of superconductivity known as topological superconductivity (TSC)¹. Molecular beam epitaxy (MBE) has been the primary approach in the scalable synthesis of the TI/superconductor heterostructures. Although the growth of epitaxial TI films on *s*-wave superconductors has been achieved²⁻⁴, it remains an outstanding challenge for synthesizing atomically thin TI/superconductor heterostructures, which are

critical for engineering the TSC phase. Here, we used MBE to grow Bi_2Se_3 films with the controlled thickness on monolayer NbSe_2 and performed *in-situ* angle-resolved photoemission spectroscopy and *ex-situ* magneto-transport measurements on these Bi_2Se_3 /monolayer NbSe_2 heterostructures. We found that the emergence of Rashba-type bulk quantum well bands and spin-nondegenerate surface states coincides with a marked suppression of the in-plane upper critical magnetic field of the superconductivity in Bi_2Se_3 /monolayer NbSe_2 heterostructures. This is the signature of a crossover from Ising- to Rashba-type superconducting pairings, induced by altering Bi_2Se_3 film thickness. Our work opens a new route for exploring a robust TSC phase in TI/Ising superconductor heterostructures.

Main text: Since the discovery of heavy-fermion superconductors and high-temperature superconductors in cuprate-perovskite ceramics, research on unconventional (i.e. non-*s*-wave) superconductivity continues to reveal new questions and challenges. An exciting possibility is topological superconductivity (TSC) in hybrid structures where a topological insulator (TI) is proximally coupled to a conventional *s*-wave superconductor¹. A primary barrier to the growth of TI films on *s*-wave superconductors (or vice versa) lies in the difficulty of achieving an atomically sharp interface due to a host of experimental challenges such as chemical reactivity and uncontrolled nucleation. To date, the most successful realization of TIs interfaced with *s*-wave superconductors is the molecular beam epitaxy (MBE)-grown Bi_2Se_3 or Bi_2Te_3 films on bulk crystals of superconducting NbSe_2 (Refs.²⁻⁶). However, for device fabrication and potential application in topological quantum computations, MBE-grown NbSe_2 films are preferred over NbSe_2 bulk crystals.

Prior studies have demonstrated that the superconductivity in atomically thin, particularly monolayer NbSe₂ films persists under in-plane magnetic fields far beyond the Pauli limit (H_p) due to its Ising-type superconducting pairing symmetry^{7,8}. In Ising-type superconductors, electron spins are pinned to the out-of-plane direction due to the breaking of SU(2) spin rotation via the strong Ising-type spin-orbit interaction. This property makes the breaking of Cooper pairs difficult under an in-plane magnetic field. The TSC phase has also been theoretically predicted in Ising-type superconductors, particularly in transition metal dichalcogenides⁹⁻¹¹. We may anticipate that a robust TSC phase appears in a TI/Ising superconductor (e.g. Bi₂Se₃/monolayer NbSe₂) heterostructure due to its complex spin-orbit coupling form. However, experimental studies along this direction are to date lacking, primarily because the Ising-type superconductor becomes non-superconducting after being covered by a TI film.

In this work, we used MBE to fabricate Bi₂Se₃/monolayer NbSe₂ heterostructures with different Bi₂Se₃ thicknesses and performed *in-situ* angle-resolved photoemission spectroscopy (ARPES) and *ex-situ* electrical transport on these heterostructures. We observed that the Dirac surface states (SSs) emerge when the thickness of Bi₂Se₃ is greater than 3 quintuple layers (QLs), which is reduced compared with previous studies of thicker (i.e. ≥ 6 QL) Bi₂Se₃ films grown on sapphire¹², bilayer graphene¹³, and Si(111) (Ref.¹⁴) substrates. We found that Rashba-type conduction bands and spin-nondegenerate Dirac SSs appear when the Bi₂Se₃ thickness is greater than 2 QL. These features observed in ARPES studies were found to agree well with our first-principles calculations. Moreover, we found that the in-plane upper critical magnetic field (i.e., $H_{c2,\parallel}/H_p$) of the superconducting Bi₂Se₃/monolayer NbSe₂ heterostructures is greatly reduced when the Rashba-type bulk conduction bands and Dirac SSs emerge, implying the crossover from the Ising- to Rashba-type superconductivity. The establishment of the MBE growth of

Bi_2Se_3 /monolayer NbSe_2 heterostructures and the demonstration of the crossover from 2D Ising- to 3D bulk Rashba-type superconductivity in these heterostructures will facilitate the investigations of the robust TSC phase in TI/Ising-type superconductor heterostructures.

The 2H phase of NbSe_2 bulk crystal is a well-studied *s*-wave superconductor¹⁵. Its unit cell consists of the Se-Nb-Se trilayer structure. The monolayer NbSe_2 has an out-of-plane mirror symmetry but breaks the in-plane inversion symmetry, which leads to Ising-type superconductivity in monolayer NbSe_2 ^{7,8}. Bi_2Se_3 is a prototypical 3D TI, wherein a single Dirac cone exists at the Γ point of the first Brillouin zone^{16,17}. The unit cell of Bi_2Se_3 consists of the Se-Bi-Se-Bi-Se QL structure. Since both NbSe_2 and Bi_2Se_3 are Se-based layered materials and share the same hexagonal lattice structure, it is natural to use MBE to synthesize both NbSe_2 and Bi_2Se_3 layers to form $\text{Bi}_2\text{Se}_3/\text{NbSe}_2$ heterostructures (Figs.1a and S1). However, as noted above, the superconductivity of MBE-grown NbSe_2 films usually fades away after the coverage of Bi_2Se_3 films. By carefully optimizing the growth protocols (see Methods), we successfully retained the superconductivity in Bi_2Se_3 /monolayer NbSe_2 heterostructures. We first characterized Bi_2Se_3 /monolayer NbSe_2 heterostructures using annular dark-field scanning transmission electron microscopy (ADF-STEM), as shown in Figs. 1b and S2. In addition to the prominent Bi_2Se_3 QL and NbSe_2 trilayer structures, we observed a BiSe bilayer with a cubic lattice structure at the $\text{Bi}_2\text{Se}_3/\text{NbSe}_2$ interface. This observation is consistent with prior studies on Bi_2Se_3 /bulk NbSe_2 (Ref.¹⁸). The formation of this cubic BiSe layer is presumably stabilized by the large work function of the monolayer NbSe_2 underneath.

As noted above, monolayer NbSe_2 is an Ising-type superconductor^{7,8}, in which the broken in-plane inversion symmetry can generate an out-of-plane spin polarization under an effective Zeeman field (i.e. Ising-type spin-orbit interaction), which induces a Zeeman-type spin splitting at

bulk valence band maxima located at K and K' points with opposite signs (Fig.1c). Therefore, the inter-valley Cooper pairs in the monolayer NbSe₂ involve two electrons with locked opposite out-of-plane spins, which are referred to as Ising-type pairing. Superconductivity can also arise in materials with a Rashba-type band structure, where the spins of the electrons are pinned to the in-plane direction (Fig.1d). Cooper pairing between two such electrons with opposite in-plane spins is known as Rashba-type pairing. In our experiment, by depositing Bi₂Se₃ films on top of monolayer NbSe₂, Rashba-type conduction bands and Dirac SSs emerge and become superconducting due to the proximity effect. Therefore, Bi₂Se₃/monolayer NbSe₂ heterostructures provide a platform to study the crossover between Ising- and Rashba-type pairings in a single system.

We next performed *in-situ* ARPES measurements on m QL Bi₂Se₃/monolayer NbSe₂ heterostructures with systematically increasing m . For monolayer NbSe₂ (i.e. $m = 0$), a hole pocket that crosses the Fermi energy near the Γ point was observed (Fig. S3), consistent with prior studies^{19,20}. After deposition of 1 QL Bi₂Se₃ (i.e. $m = 1$) on monolayer NbSe₂, the ARPES band map shows a near-parabolic band dispersion, which is analogous to that of the 1 QL Bi₂Se₃ directly grown on epitaxial bilayer graphene substrates¹³. Compared to 1 QL Bi₂Se₃ grown on graphene, the 1 QL Bi₂Se₃/monolayer NbSe₂ is more electron-doped. The bulk conduction band minimum is at $(E-E_F) \sim -0.55$ eV (Figs. 2a and 2g). A gap of ~ 0.73 eV was observed for the $m = 1$ sample (Fig. S3). With increasing m , the hybridization gap between the top and bottom SSs decreases. The gap is ~ 0.18 eV for the $m = 2$ sample. Furthermore, we observed Rashba-type SSs for the $m = 2$ sample (Figs. 2b and 2h), implying symmetry-inequivalent top and bottom SSs (Ref. ¹³). For the $m \geq 3$ samples, the SSs become gapless, a signature of crossover from 2D to 3D TI regimes (Figs. 2c and 2i)²¹. The crossover thickness in Bi₂Se₃/NbSe₂ heterostructures is found to

be 3 QL. This is significantly lower than the 6 QL observed for Bi₂Se₃ films grown on other substrates including NbSe₂ bulk crystals^{2,3,12-14}. With increasing m , the chemical potential gradually approaches the Dirac point (Figs. 2d to 2f and 2j to 2l).

In addition to the reduced 2D to 3D crossover thickness, the bulk conduction bands of Bi₂Se₃ films grown on monolayer NbSe₂ form quantum well (QW) states for $m \geq 2$ (Figs. 2b to 2f and 2h to 2l). Distinct from the QW states observed in Bi₂Se₃ films on sapphire¹², bilayer graphene¹³, Si(111)¹⁴, and NbSe₂ bulk crystals^{2,3}, the QW states in m QL Bi₂Se₃/monolayer NbSe₂ heterostructures exhibit a Rashba-type band splitting, similar to a recent theoretical prediction based on Bi₂Se₃/monolayer PtSe₂ heterostructures²². To estimate the Rashba coupling strength α_R of the lowest QW states (labeled QW1 in Fig. 2), we defined the energy difference between the minimum of QW1 states and Rashba band crossing at the Γ point as E_R and the momentum offset of two Rashba bands as k_R (Fig. 2b). Consequently, the Rashba splitting parameter for a local parabolic dispersion is approximated by $\alpha_R = 2E_R/k_R$. For the $m = 2$ sample, $E_R \sim 0.019$ eV and $k_R \sim 0.038 \text{ \AA}^{-1}$, yielding $\alpha_R \sim 1.0 \text{ eV} \cdot \text{\AA}$. The value of α_R in the 2 QL Bi₂Se₃/monolayer NbSe₂ heterostructure is comparable to that of the Rashba splitting of Bi₂Se₃ bulk conduction QW states²³⁻²⁶. With increasing m , α_R decreases monotonically and almost vanishes in the $m = 6$ sample, but the Rashba splitting of the second-lowest bulk QW states (labeled QW2 in Fig. 2) remains large in the $3 \leq m \leq 6$ samples (Figs. 2 and S4). The appearance of Rashba-type bulk QW bands and/or spin-nondegenerate Dirac SSs can together influence the occurrence of the superconducting proximity effect between Bi₂Se₃ and monolayer NbSe₂ films, as discussed below.

Next, we focused on transport measurements of m QL Bi₂Se₃/monolayer NbSe₂ heterostructures. As shown in Fig. 2, the chemical potential crosses the Rashba-type bulk bands and/or spin-nondegenerate Dirac SSs, the electrons possess in-plane spin-polarization in both cases

(Fig. 1d). When the superconducting proximity effect occurs between monolayer NbSe₂ film and m QL Bi₂Se₃ films, the Ising-type pairing in monolayer NbSe₂ film is suppressed and the Rashba-type pairing becomes progressively dominant with increasing m in m QL Bi₂Se₃/monolayer NbSe₂ heterostructures. Figure 3a shows the temperature dependence of the normalized longitudinal resistance R of the m QL Bi₂Se₃/NbSe₂ heterostructures with $0 \leq m \leq 6$. All these samples show superconductivity, with the superconducting transition temperatures (T_c) decreasing with increasing m . Here, we defined T_c as the temperature at which R drops to 50% of the normal state resistance found at $T = 5$ K. T_c is found to decrease from ~ 2.8 K for the monolayer NbSe₂ to ~ 0.6 K for the $m = 6$ sample²⁷ (Fig. S5). Note that our ARPES band map of the $m = 1$ heterostructure shows a superposition of the electronic band structures of both 1 QL Bi₂Se₃ and monolayer NbSe₂ (Fig. S3). Since the valence band alignment of monolayer NbSe₂ does not change in the $m = 0$ and $m = 1$ samples, we can ignore the charge transfer effect between Bi₂Se₃ and monolayer NbSe₂ layers. Therefore, the observed superconductivity suppression (i.e. T_c reduction) in our Bi₂Se₃/monolayer NbSe₂ heterostructures can be primarily attributed to the standard superconducting proximity effect²⁸ (Fig. S6) rather than the electron injection across the interface between Bi₂Se₃ and monolayer NbSe₂ layers²⁹.

We performed the magnetoresistance measurements on these Bi₂Se₃/monolayer NbSe₂ heterostructures under in-plane and out-of-plane magnetic fields (Figs. 3b and 3c). The upper critical magnetic fields $H_{c2,\parallel}$ and $H_{c2,\perp}$ are defined as the magnetic field at which R is $\sim 50\%$ of the normal state resistance (Figs. S7 to S9). Figure 3b shows the reduced temperature (T/T_c) dependence of the normalized in-plane upper critical magnetic field ($H_{c2,\parallel}/H_P$) for the m QL Bi₂Se₃/monolayer NbSe₂ heterostructures with $0 \leq m \leq 6$. For the $m = 0$ sample, the ($H_{c2,\parallel}/H_P$) $\sim(T/T_c)$ curve near T_c can be fitted by using $H_{c2,\parallel}/H_P \propto \sqrt{1 - T/T_c}$ for a 2D superconductor.

When 1 QL Bi₂Se₃ is deposited on top of monolayer NbSe₂, i.e. the $m = 1$ sample, the $(H_{c2,\parallel}/H_P) \sim (T/T_c)$ curve deviates slightly from this square-root- T behavior, indicating a crossover from 2D to 3D superconductivity³⁰. For the $m \geq 2$ samples, the $(H_{c2,\parallel}/H_P) \sim (T/T_c)$ curves can be fitted with $H_{c2,\parallel}/H_P \propto (1 - T/T_c)$ for a 3D superconductor. The linear temperature dependence of $H_{c2,\parallel}$ indicates that the orbital effect is dominant rather than the paramagnetic effect for the in-plane pair-breaking magnetic field in the Bi₂Se₃/NbSe₂ heterostructures with $m \geq 2$. Given the presence of the Rashba-type conduction bands and spin-nondegenerate Dirac SSs, the bulk Rashba-type superconductivity may appear in the $m \geq 2$ samples. Next, we extrapolated the value of $H_{c2,\parallel}/H_P$ at $T = 0$ K from the $(H_{c2,\parallel}/H_P) \sim (T/T_c)$ curves. In the monolayer NbSe₂, the extracted $H_{c2,\parallel}(T = 0\text{K})$ is greater than 4.9 times the Pauli limit H_P , confirming the Ising-type pairing in monolayer NbSe₂. By depositing m QL Bi₂Se₃ films on the monolayer NbSe₂, $H_{c2,\parallel}(T = 0\text{K})/H_P$ is reduced to ~ 3.4 for $m = 1$ and ~ 2.0 for $2 \leq m \leq 6$. The value of $H_{c2}(T = 0\text{K})/H_P$ greater than the factor of $\sqrt{2}$ in the $2 \leq m \leq 6$ samples provides further evidence that bulk Rashba-type superconductivity takes over from Ising-type behavior in Bi₂Se₃/monolayer NbSe₂ heterostructures³¹.

The temperature dependence of $H_{c2,\perp}$ provides additional insights into the superconductivity in Bi₂Se₃/monolayer NbSe₂ heterostructures. We found that the $H_{c2,\perp} \sim (T/T_c)$ curves display a linear behavior in both monolayer NbSe₂ and m QL Bi₂Se₃/monolayer NbSe₂ heterostructures due to the constraint of the orbital pair-breaking effect (Fig. 3c). As noted above, the Rashba-type superconductivity emerges in the $2 \leq m \leq 6$ samples, where the spins of two electrons are pinned to the in-plane direction (Fig. 1d). However, with an out-of-plane magnetic field, the orbital effect dominates, allowing the breaking of Cooper pairing. As a consequence, the enhancement of

$H_{c2,\perp}$ was not observed in these bulk Rashba-type superconductors (Fig. 3c). We used the Ginzburg-Landau (GL) expression $H_{c2,\perp} = \Phi/(2\pi\xi_{GL,\perp}^2)$ to calculate the out-of-plane GL coherence length $\xi_{GL,\perp}$ from $H_{c2,\perp}(T = 0K)$. Here Φ is the magnetic flux quantum. The value determined for the monolayer NbSe₂, $\xi_{GL,\perp} \sim 14$ nm, is consistent with that found in bulk NbSe₂ crystals⁴. The value of $\xi_{GL,\perp}$ increases continuously with increasing m , suggesting the proximity-induced superconductivity occurs on both the interior and the top surface of the Bi₂Se₃ films even in the $m = 6$ sample. A proximity-induced superconducting gap on both the top and bottom Dirac SSs is a prerequisite for creating the TSC phase in TI/superconductor heterostructures¹. For the $m = 6$ sample, $\xi_{GL,\perp}$ is found to be ~ 57 nm (Fig. 3c inset). A similar enhancement of $\xi_{GL,\perp}$ has been observed in proximity-induced superconductivity in Bi₂Te₃/bulk NbSe₂ heterostructures⁴. As a result, we posited that the proximity-induced superconducting gap occurs in both the Rashba-type bulk bands and spin-nondegenerate Dirac SSs of the Bi₂Se₃ layer. This leads to bulk Rashba-type superconductivity in the $m \geq 2$ samples. In addition to $\xi_{GL,\perp}$, the in-plane GL coherence length $\xi_{GL,\parallel}$ deduced from $H_{c2,\parallel}(T = 0K)$ also continuously increases with increasing m , further confirming the appearance of the proximity-induced superconductivity on the top surface of TI films (Fig. 3b inset).

To understand our transport results, we theoretically analyzed $H_{c2,\parallel}$ by considering the Zeeman coupling of monolayer NbSe₂. The Ising-type superconductivity in monolayer NbSe₂ serves as the Cooper pairing source for the bulk superconductivity in m QL Bi₂Se₃/NbSe₂ heterostructures. A strong Ising-type spin-orbit coupling ($\beta_{so} \sim 1.75$ meV) protects the superconducting states against the depairing term of the in-plane magnetic field, which gives rise to a large $H_{c2,\parallel}/H_P$. The enhanced paramagnetic limit³² is described by

$$\text{Log} \left[\frac{T}{T_c} \right] = \text{Re} \left[\psi^{(0)} \left(\frac{1}{2} \right) - \psi^{(0)} \left(\frac{1}{2} + i \frac{\sqrt{\beta_{so}^2 + H_x^2}}{2\pi k_B T} \right) \right] \times \frac{H_x^2}{\beta_{so}^2 + H_x^2} \quad (1)$$

where $\psi^{(0)}(z)$ is the digamma function, k_B is the Boltzmann constant, and H_x is the Zeeman energy. We first used Eq. (1) to fit the $(H_{c2,\parallel}/H_P) \sim (T/T_c)$ curves of the monolayer NbSe₂ film with a single Ising-type spin-orbit coupling parameter β_{so} and achieved the best fit with $\beta_{so} \sim 1.75$ meV (Fig. 4a). We next examined the influence of Rashba-type spin-orbit coupling on the upper critical field (see Eq. (8) in Methods), and with two fitting parameters β_{so} and $\alpha_0 = \alpha_R k_F$. The Rashba parameter α_0 reduces the upper critical field, thus, with a finite α_0 , one has to also increase β_{so} to achieve a good fit. Figure 4b shows a fit for $\beta_{so} \sim 2.1$ meV with different α_0 , and the best fit is achieved with $\alpha_0 \sim 0.42$ meV, which is much smaller than β_{so} i.e., $\alpha_0 < \beta_{so}/5$. Therefore, our theoretical calculations demonstrate that the 2D superconductivity in monolayer NbSe₂ carries Ising-type dominant Cooper pairs. For the $m = 1$ sample, the temperature dependence of the upper critical magnetic field deviates from either linear- T (GL-3D limit) or square-root- T (GL-2D limit) behavior, suggesting a complicated crossover behavior from a 2D Ising-type superconductor to a 3D bulk Rashba-type superconductor in this sample (Fig. 4c). The comparison between the theoretical model calculations and experimental data for the $m = 1$ sample is shown in Fig. 4c. The experimental data fall into the regime with the Rashba parameter $\alpha_0 \approx 0.7 \sim 1.1$ meV, which is comparable to $\beta_{so} \sim 1.75$ meV. The discrepancy between theory and experiment is attributed to the 3D orbital effects that are not captured in our 2D model. In the Supplementary Information, we discussed another mechanism of intervalley scattering that can also suppress $H_{c2,\parallel}$ due to the interfacial cubic BiSe bilayer (Fig.S10).

To identify the origin of the strong Rashba effect and the concurrent reduction of 2D to 3D TI crossover thickness in *m*QL Bi₂Se₃/BiSe/monolayer NbSe₂ heterostructures, we performed first-principles calculations to examine bulk QW bands and Dirac SSs. Capturing the entire Bi₂Se₃/BiSe/NbSe₂ heterostructure in first-principles calculations is challenging because a supercell commensurate with two different hexagonal lattices and a third cubic one is required. We instead examined two pairs of BiSe/NbSe₂ and Bi₂Se₃/BiSe. The electronic structure of BiSe/monolayer NbSe₂ shows that the band filling occupation of the monolayer NbSe₂ layer does not show any significant change ($\sim 0.04e$ per NbSe₂ formula unit) (Fig. S11), consistent with our ARPES observation (Fig. S3). This insignificant charge transfer across BiSe/NbSe₂ leaves the hole carriers in the NbSe₂ layer uncompensated, which can still support the presence of superconductivity. Therefore, our following calculation of Bi₂Se₃/BiSe is a valid structural approximation of the *m*QL Bi₂Se₃/BiSe/monolayer NbSe₂ heterostructures.

Figure 4d shows the orbital-projected band structure of the 3QL Bi₂Se₃/BiSe heterostructure. For $-0.6 \text{ eV} \leq (E - E_F) \leq -0.4 \text{ eV}$, two Dirac SSs appear at different energies. The upper SS remains mostly intact, localized at the upper surface, while the lower SS drops to a lower energy level due to its interaction with the BiSe layer but has an increased decay length (Figs. 4e and S12). Therefore, we can attribute the energy separation of the two Dirac SSs to the interaction between the lower Dirac SS and the BiSe layer, which relieves the lower Dirac SS from further hybridizing with the upper Dirac SS. This explains why the critical thickness for the 2D to 3D TI crossover in Bi₂Se₃/monolayer NbSe₂ heterostructures is reduced. For $-0.25 \text{ eV} \leq (E - E_F) \leq 0 \text{ eV}$, three QW bands labeled as QW1, QW2, and QW3 appear, consistent with their *xy*-plane-averaged partial charge densities having 0, 1, and 2 nodes (Fig.4f). QW1 and QW2 are located at $\sim 0.22 \text{ eV}$ and $\sim 0.39 \text{ eV}$ above the Dirac point of the upper SS, respectively, in good agreement with

~ 0.23 eV and ~ 0.44 eV determined from the ARPES band map of the $m = 3$ sample (Figs. 2c and 2i). The calculated Rashba splitting E_R of QW1 is ~ 0.009 eV (Fig. S13), which is also close to the value of $E_R \sim 0.011$ eV measured by ARPES. Since m QL Bi_2Se_3 films usually produce $(m - 1)$ QW states to the conduction band minimum (Fig. S14), the three QW states suggest that the $m = 3$ sample is effectively equivalent to a freestanding 4QL Bi_2Se_3 sample (Fig. S15). In other words, the BiSe layer electronically resembles an additional Bi_2Se_3 layer. This is further confirmed by comparing the three QW states in the 3QL $\text{Bi}_2\text{Se}_3/\text{BiSe}$ heterostructure with those in the freestanding 4QL Bi_2Se_3 sample (Fig. 4g). However, the 3QL $\text{Bi}_2\text{Se}_3/\text{BiSe}$ heterostructure is different from the freestanding 4QL Bi_2Se_3 because the crystal potential of the former structure is asymmetric along z , as reflected from their partial charge densities plotted along z in Fig. 4g. Therefore, the presence of the interfacial BiSe layer facilitates the formation of bulk Rashba-type QW bands with large α_R by introducing a compositional gradient along z (Fig. S16).

In summary, we fabricated superconducting $\text{Bi}_2\text{Se}_3/\text{monolayer NbSe}_2$ heterostructures by MBE and found that an interfacial BiSe layer with a cubic lattice structure is formed at the interface between Bi_2Se_3 and monolayer NbSe_2 layers. By performing *in-situ* ARPES measurements, we observed the formation of gapless Dirac SSs in the 3 QL $\text{Bi}_2\text{Se}_3/\text{monolayer NbSe}_2$ heterostructure. Moreover, several bulk Rashba-type QW bands appear in $\text{Bi}_2\text{Se}_3/\text{monolayer NbSe}_2$ heterostructures with Bi_2Se_3 thickness greater than 2 QL. By performing magnetoresistance measurements, we found that both in-plane and out-of-plane upper critical magnetic fields of the superconducting $\text{Bi}_2\text{Se}_3/\text{monolayer NbSe}_2$ heterostructures are greatly reduced with increasing the Bi_2Se_3 film thickness, indicating the occurrence of a crossover from Ising- to bulk Rashba-type pairings. The successful synthesis of both an Ising-type superconductor and TI films by MBE and

the observation of the crossover from Ising-type to bulk Rashba-type superconductivity may advance the exploration of the robust TSC phase in TI/Ising-type superconductor heterostructures.

Methods

MBE growth of Bi₂Se₃/monolayer NbSe₂ heterostructures

The Bi₂Se₃/monolayer NbSe₂ heterostructures used in this work were grown on the bilayer graphene terminated 6H-SiC (0001) substrates in a MBE chamber (ScientaOmicron) with a vacuum better than 2×10^{-10} mbar. For the MBE growth of monolayer NbSe₂, the substrate temperature was kept at 500°C. The monolayer NbSe₂ was post-annealed at 600 °C for 30 minutes to improve its crystallinity. Next, the Bi₂Se₃ films were grown on monolayer NbSe₂ at ~150°C. This low growth temperature is crucial for achieving the superconductivity in Bi₂Se₃/monolayer NbSe₂ heterostructures. The MBE growth process was monitored by the reflection high-energy electron diffraction (RHEED) (Fig. S1). The samples were capped with a 10 nm Se layer to prevent their degradation during the *ex-situ* electrical transport measurements.

ADF-STEM measurements

The Aberration-corrected ADF-STEM measurements were performed on an FEI Titan³ G2 STEM operating at an accelerating voltage of 300 kV, with a probe convergence angle of 25 mrad, a probe current of 100 pA, and ADF detector angles of 42~244 mrad. See more STEM images of Bi₂Se₃/monolayer NbSe₂ heterostructures in Fig. S2.

ARPES measurements

The *in-situ* ARPES measurements were performed at room temperature after transferring the samples from the MBE chamber. A hemispherical Scienta DA30L analyzer was used, and the

photoelectrons were excited by a helium discharged lamp with a photon energy of ~ 21.2 eV. The energy and angle resolution were set at ~ 10 meV and $\sim 0.1^\circ$, respectively.

Electrical transport measurements

The electrical transport measurements were carried out in a Physical Property Measurement System (Quantum Design DynaCool, 2 K, 9 T), a Heliox He³ refrigerator (Oxford Instruments, 400 mK, 6 T), and a dilution refrigerator (Bluefors, 20 mK, 9-1-1 T). Six-terminal mechanically defined Hall bars were used for electrical transport studies.

First-principles calculations

The first-principles calculations were performed using the Perdew-Burke-Ernzerhof (PBE) parametrization of the generalized gradient approximation exchange-correlation functional³³. Interactions between electrons and nuclei were described by the projector augmented wave pseudopotentials³⁴ as implemented in the Vienna Simulation Package (VASP)³⁵. Interlayer van der Waals interactions were accounted for using Grimme's DFT-D3 correction scheme³⁶. Noncollinear spin textures and spin-orbit coupling were enabled following the native VASP implementation. Convergence parameters included the following: a plane-wave expansion energy cutoff of 500 eV, a residual force threshold of 0.01 eV/Å for relaxations (except for *m* QL Bi₂Se₃ plus BiSe, see below), a 12×12×1 *k*-point grid for multilayer Bi₂Se₃ unit-cell calculations, and a 6×1×1 *k*-point grid for Bi₂Se₃ plus BiSe calculations.

For Bi₂Se₃ plus BiSe calculations, a $1 \times 3\sqrt{3}$ trilayer Bi₂Se₃ plus 1×5 cubic BiSe supercell was chosen, where Bi₂Se₃ adopted its native lattice constant of 4.14Å, requiring cubic BiSe to accommodate by sustaining a slight strain (1.6% and 2.2% in the lateral directions, considering BiSe's native lattice constant 4.21Å). This favoritism towards Bi₂Se₃ was to ensure the accuracy

of the low-energy electronic structure of the heterostructure, dominated by Bi_2Se_3 bands (to be compared with experiments), and is also justified by the larger thickness of Bi_2Se_3 than BiSe . Structural relaxations for Bi_2Se_3 plus BiSe were prematurely terminated where residual forces were still $\sim 0.2 \text{ eV/\AA}$; at this stage, the softest degrees of freedom (Bi_2Se_3 - BiSe interlayer separation) had already stabilized and resumed relaxation would strongly distort the BiSe layer through the formation of strong bonds between Bi (in BiSe) and Se (in Bi_2Se_3) wherever a $\text{Bi}(\text{BiSe})/\text{Se}(\text{Bi}_2\text{Se}_3)$ pair happened to be close in the supercell. In a realistic structure including the underlying NbSe_2 and graphene substrate, such distortions would be suppressed since they would inflict additional energy penalty in interlayer adhesion and bending at the $\text{BiSe}/\text{NbSe}_2$ interface. Although a full relaxation with a near-commensurate supercell containing all structural components (i.e. Bi_2Se_3 , BiSe , NbSe_2 , and graphene) would be ideal, it would also require >1000 atoms (with spin-orbit coupling) and is therefore beyond our computational capabilities. For this reason, we used a flat Bi_2Se_3 plus BiSe structure in all electronic structure calculations.

Theoretical calculations of critical temperature and upper critical magnetic fields

To achieve the best fit for our experimental data of the monolayer NbSe_2 sample, we took an adjustment of T_c with a 3% error from the experimental data into account. It means T_c achieved in our experiments might be replaced by

$$T'_c = T_c + \Delta T_c \quad (2)$$

From the GL theory in the 2D limit, we knew that

$$b_0 \left(\frac{H}{H_P} \right)^2 = 1 - \frac{T(H)}{T'_c} = 1 - \frac{T(H)}{T_c + \Delta T_c} \quad (3)$$

It leads to

$$\frac{T(H)}{T_c + \Delta T_c} = 1 - b_0 \left(\frac{H}{H_P} \right)^2 \quad (4)$$

which can be rewritten as

$$\frac{T(H)}{T_c} = \frac{T_c + \Delta T_c}{T_c} \left[1 - b_0 \left(\frac{H}{H_P} \right)^2 \right] \quad (5)$$

for the fitting process. Here, there are two fitting parameters b_0 and ΔT_c . During the fitting process, $|\Delta T_c|$ is less than $3\%T_c$.

In addition to the GL theory, we also adopted a model calculation to fit the in-plane upper critical field $H_{c2,\parallel}$ to reveal the role of the Ising-type spin-orbit coupling β_{so} in our experiments.

We considered the normal Hamiltonian of the monolayer NbSe₂ around K and K' valleys³² as

$$H_0 = \left(\frac{p^2}{2m_h} - \mu \right) \tau_0 s_0 + \beta_{so} \tau_z s_z + \alpha_R (p_x s_y - p_y s_x) + H_x s_x \quad (6)$$

where m_h is the effective mass and τ, s are Pauli matrices in the valley and spin subspace, respectively. A phenomenological interaction Hamiltonian is considered to induce a spin-singlet inter-valley pairing state³². Note that the spin-triplet components induced by spin-orbit coupling are in order of $\beta_{so}/\mu \ll 1$, which can be ignored for simplicity³².

To study the relationship between the in-plane upper critical magnetic field $H_{c2,\parallel}$ and the critical temperature T/T_c , we used the standard GL theory and solved the linearized gap equation³⁷

$$\frac{1}{v_0} = -k_B T \sum_{i\omega_n, p} \text{Tr}[(\tau_x s_y) G_e(i\omega_n, p) (\tau_x s_y) G_h(i\omega_n, -p)] \quad (7)$$

where v_0 is the dimensionless attractive interaction strength, and $\omega_n = (2n + 1)\pi k_B T$, $G_e(i\omega_n, p) = [i\omega_n - H_0(p)]^{-1}$ is the Matsubara Green's function for electrons, and $G_h = -G_e^*$ for holes.

We first considered a simple limit with $\alpha_R = 0$, then the solution of Eq. (7) gives rise to Eq. (1), which explains why the Ising-type superconductivity is resilient to an in-plane pair-breaking magnetic field. For the monolayer NbSe₂, the best fit is achieved with $\beta_{so} = 1.75$ meV. Under a weak magnetic field, the factor $H_x^2/(\beta_{so}^2 + H_x^2) \ll 1$ induces a large in-plane $H_{c2,\parallel} \gg H_P$.

Next, we included the Rashba-type spin-orbit coupling α_0 which competes with β_{so} (Ref.³²), the solution of Eq. (7) becomes

$$\text{Log} \left[\frac{T}{T_c} \right] = \frac{1}{2} [C_0(\rho_-) + C_0(\rho_+)] + \frac{1}{2} [C_0(\rho_-) - C_0(\rho_+)] \times \frac{\beta_{so}^2 + \alpha_0^2 - H_x^2}{E_- E_+} \quad (8)$$

where $E_{\pm} = \sqrt{\beta_{so}^2 + (H_x \pm \alpha_0)^2}$ with $\alpha_0 = \alpha_R k_F$ and k_F is the Fermi momentum, $\rho_{\pm} = \frac{1}{2}(E_+ \pm E_-)$. The kernel of the de-pairing function in Eq. (8) is given by $C_0(x) = \text{Re} \left[\psi^{(0)} \left(\frac{1}{2} \right) - \psi^{(0)} \left(\frac{1}{2} + i \frac{x}{2\pi k_B T} \right) \right]$ with $\psi^{(0)}(z)$ the digamma function. Note that Eq. (8) can be reduced to Eq. (1) in the main text by setting $\alpha_0 = 0$. The presence of α_R increases the depairing term ρ_{\pm} which in turn decreases the in-plane $H_{c2,\parallel}$. However, through fitting the experimental data of the monolayer NbSe₂ sample, we found that the Rashba-type spin-orbit coupling energy α_0 is much smaller than the Ising-type spin-orbit coupling β_{so} , i.e., $\alpha_0 < \beta_{so}/5$, and thus the Rashba effect can be ignored in the monolayer NbSe₂ (Fig. 4b). Finally, we used Eq. (8) to investigate the paramagnetic pair-breaking effect for the $m = 1$ sample. The moderate fit shows $\beta_{so} = 1.75$ meV and $\alpha_0 = 0.9$ meV (Fig. 4c), these two comparable spin-orbit couplings indicate the occurrence of the crossover from Ising-type (i.e. the $m = 0$ sample) to Rashba-type (i.e. the $m \geq 2$ sample) Copper pairs in Bi₂Se₃/monolayer NbSe₂ heterostructures.

Acknowledgments

We thank Yongtao Cui, K. T. Law, and Di Xiao for helpful discussions. This work is primarily supported by the Penn State MRSEC for Nanoscale Science (DMR-2011839). The electrical transport measurements and the sample characterization are partially supported by the NSF-CAREER award (DMR-1847811). The theoretical calculations and simulations are partially supported by the DOE grant (DE-SC0019064). Y. W. acknowledges the support from a startup

grant from the University of North Texas. The MBE growth and the ARPES measurements were performed in the NSF-supported 2DCC MIP facility (DMR-2039351). The dilution refrigerator transport measurements at U. Washington are supported by the AFOSR award (FA9550-21-1-0177) and acknowledge the usage of the millikelvin optoelectronic quantum material laboratory supported by the M. J. Murdock Charitable Trust. D.R.H and N.A. acknowledge the support from the NSF-CAREER award (DMR-1654107). C. -Z. C. also acknowledges the support from the Gordon and Betty Moore Foundation's EPiQS Initiative (Grant GBMF9063 to C. -Z. C.).

Author contributions: C.-Z. C. conceived and designed the experiment. H. Y. performed the MBE growth, ARPES, and PPMS transport measurements with the help of Y.-F. Z, L-J. Z., R. Z, A. R. R., M. H. W. C., N. S., and C.-Z. C.. R. X. and H. Y. performed the Helium-3 transport measurements with the help of N. S. and C.-Z. C.. J. C. and X. X. performed the dilution transport measurements. Y. W. performed first-principles calculations. C. D. and J. A. R. prepared the bilayer graphene-terminated 6H-SiC(0001) substrates. D. R. H. and N. A. carried out the TEM measurements. L.-H. H. and C.-X. L. performed the theoretical simulations. H. Y., L.-H. H., Y. W., and C. -Z. C. analyzed the data and wrote the manuscript with inputs from all authors.

Competing interests: The authors declare no competing interests.

Data availability: The datasets generated during and/or analyzed during this study are available from the corresponding author upon reasonable request.

Code availability: The codes used in theoretical simulations and calculations are available from the corresponding author upon reasonable request.

References

- 1 Fu, L. & Kane, C. L. Superconducting Proximity Effect and Majorana Fermions at the Surface of a Topological Insulator. *Phys. Rev. Lett.* **100**, 096407 (2008).
- 2 Wang, M. X., Liu, C. H., Xu, J. P., Yang, F., Miao, L., Yao, M. Y., Gao, C. L., Shen, C. Y., Ma, X. C., Chen, X., Xu, Z. A., Liu, Y., Zhang, S. C., Qian, D., Jia, J. F. & Xue, Q. K. The Coexistence of Superconductivity and Topological Order in the Bi₂Se₃ Thin Films. *Science* **336**, 52-55 (2012).
- 3 Xu, S. Y., Alidoust, N., Belopolski, I., Richardella, A., Liu, C., Neupane, M., Bian, G., Huang, S. H., Sankar, R., Fang, C., Dellabetta, B., Dai, W. Q., Li, Q., Gilbert, M. J., Chou, F. C., Samarth, N. & Hasan, M. Z. Momentum-space imaging of Cooper pairing in a half-Dirac-gas topological superconductor. *Nat. Phys.* **10**, 943-950 (2014).
- 4 Xu, J. P., Liu, C. H., Wang, M. X., Ge, J. F., Liu, Z. L., Yang, X. J., Chen, Y., Liu, Y., Xu, Z. A., Gao, C. L., Qian, D., Zhang, F. C. & Jia, J. F. Artificial Topological Superconductor by the Proximity Effect. *Phys. Rev. Lett.* **112**, 217001 (2014).
- 5 Xu, J. P., Wang, M. X., Liu, Z. L., Ge, J. F., Yang, X., Liu, C., Xu, Z. A., Guan, D., Gao, C. L., Qian, D., Liu, Y., Wang, Q. H., Zhang, F. C., Xue, Q. K. & Jia, J. F. Experimental detection of a Majorana mode in the core of a magnetic vortex inside a topological insulator-superconductor Bi₂Te₃/NbSe₂ heterostructure. *Phys. Rev. Lett.* **114**, 017001 (2015).
- 6 Sun, H. H., Zhang, K. W., Hu, L. H., Li, C., Wang, G. Y., Ma, H. Y., Xu, Z. A., Gao, C. L., Guan, D. D., Li, Y. Y., Liu, C. H., Qian, D., Zhou, Y., Fu, L., Li, S. C., Zhang, F. C. & Jia, J. F. Majorana Zero Mode Detected with Spin Selective Andreev Reflection in the Vortex of a Topological Superconductor. *Phys. Rev. Lett.* **116**, 257003 (2016).
- 7 Xi, X. X., Wang, Z. F., Zhao, W. W., Park, J. H., Law, K. T., Berger, H., Forro, L., Shan, J. & Mak, K. F. Ising pairing in superconducting NbSe₂ atomic layers. *Nat. Phys.* **12**, 139-143 (2016).
- 8 Xing, Y., Zhao, R., Shan, P. J., Zheng, F. P., Zhang, Y. W., Fu, H. L., Liu, Y., Tian, M. L., Xi, C. Y., Liu, H. W., Feng, J., Lin, X., Ji, S. H., Chen, X., Xue, Q. K. & Wang, J. Ising Superconductivity and Quantum Phase Transition in Macro-Size Monolayer NbSe₂. *Nano Lett.* **17**, 6802-6807 (2017).
- 9 Hsu, Y. T., Vaezi, A., Fischer, M. H. & Kim, E. A. Topological Superconductivity in Monolayer Transition Metal Dichalcogenides. *Nat. Commun.* **8**, 14985 (2017).

- 10 Xu, G., Wang, J., Yan, B. H. & Qi, X. L. Topological superconductivity at the edge of transition-metal dichalcogenides. *Phys. Rev. B* **90**, 100505 (2014).
- 11 Zhou, B. T., Yuan, N. F. Q., Jiang, H. L. & Law, K. T. Ising superconductivity and Majorana fermions in transition-metal dichalcogenides. *Phys. Rev. B* **93**, 180501 (2016).
- 12 Chang, C. Z., He, K., Wang, L. L., Ma, X. C., Liu, M. H., Zhang, Z. C., Chen, X., Wang, Y. Y. & Xue, Q. K. Growth of Quantum Well Films of Topological Insulator Bi₂Se₃ on Insulating Substrate. *SPIN* **1**, 21-25 (2011).
- 13 Zhang, Y., He, K., Chang, C. Z., Song, C. L., Wang, L. L., Chen, X., Jia, J. F., Fang, Z., Dai, X., Shan, W. Y., Shen, S. Q., Niu, Q., Qi, X. L., Zhang, S. C., Ma, X. C. & Xue, Q. K. Crossover of the Three-Dimensional Topological Insulator Bi₂Se₃ to the Two-Dimensional Limit. *Nat. Phys.* **6**, 584-588 (2010).
- 14 Sakamoto, Y., Hirahara, T., Miyazaki, H., Kimura, S. & Hasegawa, S. Spectroscopic evidence of a topological quantum phase transition in ultrathin Bi₂Se₃ films. *Phys. Rev. B* **81**, 165432 (2010).
- 15 Yokoya, T., Kiss, T., Chainani, A., Shin, S., Nohara, M. & Takagi, H. Fermi surface sheet-dependent superconductivity in 2H-NbSe₂. *Science* **294**, 2518-2520 (2001).
- 16 Zhang, H. J., Liu, C. X., Qi, X. L., Dai, X., Fang, Z. & Zhang, S. C. Topological Insulators in Bi₂Se₃, Bi₂Te₃ and Sb₂Te₃ with a Single Dirac Cone on the Surface. *Nat. Phys.* **5**, 438-442 (2009).
- 17 Xia, Y., Qian, D., Hsieh, D., Wray, L., Pal, A., Lin, H., Bansil, A., Grauer, D., Hor, Y. S., Cava, R. J. & Hasan, M. Z. Observation of a Large-Gap Topological-Insulator Class with a Single Dirac Cone on the Surface. *Nat. Phys.* **5**, 398-402 (2009).
- 18 Wang, M. X., Li, P., Xu, J. P., Liu, Z. L., Ge, J. F., Wang, G. Y., Yang, X. J., Xu, Z. A., Ji, S. H., Gao, C. L., Qian, D., Luo, W. D., Liu, C. H. & Jia, J. F. Interface structure of a topological insulator/superconductor heterostructure. *New J. Phys.* **16**, 123043 (2014).
- 19 Ugeda, M. M., Bradley, A. J., Zhang, Y., Onishi, S., Chen, Y., Ruan, W., Ojeda-Aristizabal, C., Ryu, H., Edmonds, M. T., Tsai, H. Z., Riss, A., Mo, S. K., Lee, D. H., Zettl, A., Hussain, Z., Shen, Z. X. & Crommie, M. F. Characterization of collective ground states in single-layer NbSe₂. *Nat. Phys.* **12**, 92-97 (2016).

- 20 Xu, C. Z., Wang, X. X., Chen, P., Flototto, D., Hlevyack, J. A., Lin, M. K., Bian, G., Mo, S. K. & Chiang, T. C. Experimental and theoretical electronic structure and symmetry effects in ultrathin NbSe₂ films. *Phys. Rev. Mater.* **2**, 064002 (2018).
- 21 Liu, C. X., Zhang, H., Yan, B. H., Qi, X. L., Frauenheim, T., Dai, X., Fang, Z. & Zhang, S. C. Oscillatory Crossover from Two-Dimensional to Three-Dimensional Topological Insulators. *Phys. Rev. B* **81**, 041307 (2010).
- 22 Sattar, S. & Larsson, J. A. Tunable Electronic Properties and Large Rashba Splittings Found in Few-Layer Bi₂Se₃/PtSe₂ Van der Waals Heterostructures. *ACS Appl. Electron. Mater.* **2**, 3585-3592 (2020).
- 23 Zhu, Z. H., Levy, G., Ludbrook, B., Veenstra, C. N., Rosen, J. A., Comin, R., Wong, D., Dosanjh, P., Ubaldini, A., Syers, P., Butch, N. P., Paglione, J., Elfimov, I. S. & Damascelli, A. Rashba Spin-Splitting Control at the Surface of the Topological Insulator Bi₂Se₃. *Phys. Rev. Lett.* **107**, 186405 (2011).
- 24 Valla, T., Pan, Z. H., Gardner, D., Lee, Y. S. & Chu, S. Photoemission Spectroscopy of Magnetic and Nonmagnetic Impurities on the Surface of the Bi₂Se₃ Topological Insulator. *Phys. Rev. Lett.* **108**, 117601 (2012).
- 25 King, P. D. C., Hatch, R. C., Bianchi, M., Ovsyannikov, R., Lupulescu, C., Landolt, G., Slomski, B., Dil, J. H., Guan, D., Mi, J. L., Rienks, E. D. L., Fink, J., Lindblad, A., Svensson, S., Bao, S., Balakrishnan, G., Iversen, B. B., Osterwalder, J., Eberhardt, W., Baumberger, F. & Hofmann, P. Large Tunable Rashba Spin Splitting of a Two-Dimensional Electron Gas in Bi₂Se₃. *Phys. Rev. Lett.* **107**, 096802 (2011).
- 26 Bahramy, M. S., King, P. D. C., de la Torre, A., Chang, J., Shi, M., Patthey, L., Balakrishnan, G., Hofmann, P., Arita, R., Nagaosa, N. & Baumberger, F. Emergent quantum confinement at topological insulator surfaces. *Nat. Commun.* **3**, 1159 (2012).
- 27 Buzdin, A. I. Proximity effects in superconductor-ferromagnet heterostructures. *Rev. Mod. Phys.* **77**, 935-976 (2005).
- 28 Wördenweber, R., Moshchalkov, V. V., Bending, S. J. & Tafuri, F. *Superconductors at the Nanoscale: From Basic Research to Applications*. (De Gruyter, 2017).
- 29 Xi, X. X., Berger, H., Forro, L., Shan, J. & Mak, K. F. Gate Tuning of Electronic Phase Transitions in Two-Dimensional NbSe₂. *Phys. Rev. Lett.* **117**, 106801 (2016).

- 30 Ruggiero, S. T., Barbee, T. W. & Beasley, M. R. Superconductivity in Quasi-Two-Dimensional Layered Composites. *Phys. Rev. Lett.* **45**, 1299-1302 (1980).
- 31 Yoshizawa, S., Kobayashi, T., Nakata, Y., Yaji, K., Yokota, K., Komori, F., Shin, S., Sakamoto, K. & Uchihashi, T. Atomic-layer Rashba-type superconductor protected by dynamic spin-momentum locking. *Nat. Commun.* **12**, 1462 (2021).
- 32 Lu, J. M., Zheliuk, O., Leermakers, I., Yuan, N. F. Q., Zeitler, U., Law, K. T. & Ye, J. T. Evidence for two-dimensional Ising superconductivity in gated MoS₂. *Science* **350**, 1353-1357 (2015).
- 33 Perdew, J. P., Burke, K. & Ernzerhof, M. Generalized gradient approximation made simple. *Phys. Rev. Lett.* **77**, 3865-3868 (1996).
- 34 Blochl, P. E. Projector Augmented-Wave Method. *Phys. Rev. B* **50**, 17953-17979 (1994).
- 35 Kresse, G. & Furthmuller, J. Efficient iterative schemes for ab initio total-energy calculations using a plane-wave basis set. *Phys. Rev. B* **54**, 11169-11186 (1996).
- 36 Grimme, S., Antony, J., Ehrlich, S. & Krieg, H. A consistent and accurate ab initio parametrization of density functional dispersion correction (DFT-D) for the 94 elements H-Pu. *J. Chem. Phys.* **132**, 154104 (2010).
- 37 Sigrist, M. & Ueda, K. Phenomenological Theory of Unconventional Superconductivity. *Rev. Mod. Phys.* **63**, 239-311 (1991).

Figures and figure captions

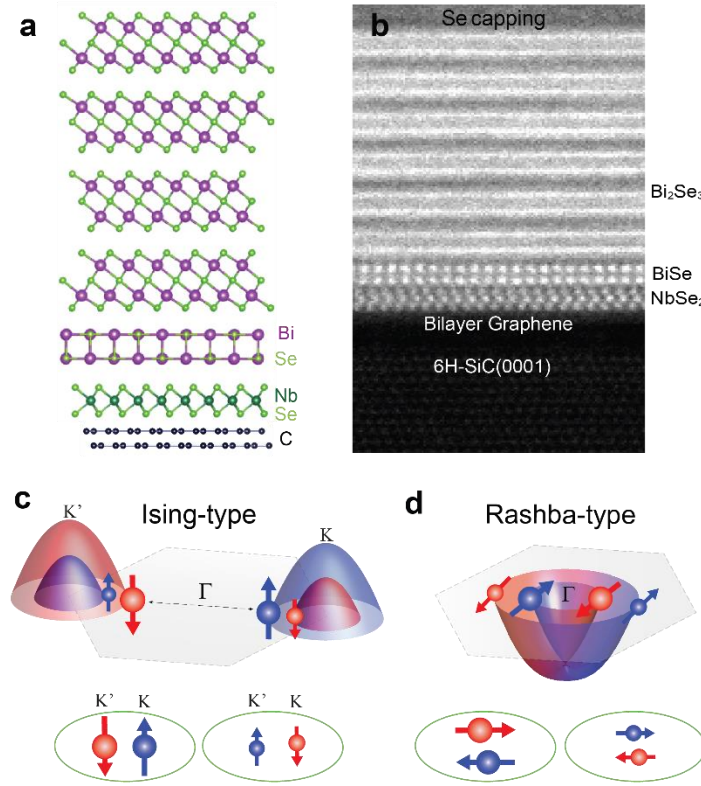


Figure 1 | MBE-grown Bi_2Se_3 /monolayer NbSe_2 heterostructures on epitaxial bilayer graphene. (a) Schematic of the 4QL Bi_2Se_3 /monolayer NbSe_2 heterostructure on bilayer graphene. (b) Cross-sectional ADF-STEM image of the 6 QL Bi_2Se_3 /monolayer NbSe_2 heterostructure on bilayer graphene. The atomic structures of monolayer NbSe_2 and Bi_2Se_3 layers can not be simultaneously resolved, suggesting a misorientation between these two layers. (c, d) Schematic of the Ising-type (c) and Rashba-type (d) pairing symmetry in superconductors. For the Ising-type superconductor (e.g. monolayer NbSe_2), the electrons near the K and K' valleys with spins pinned to the out-of-plane direction. However, for the Rashba-type superconductor (e.g. Bi_2Se_3 /monolayer NbSe_2), the electrons near the Γ point with spins pinned to the in-plane direction.

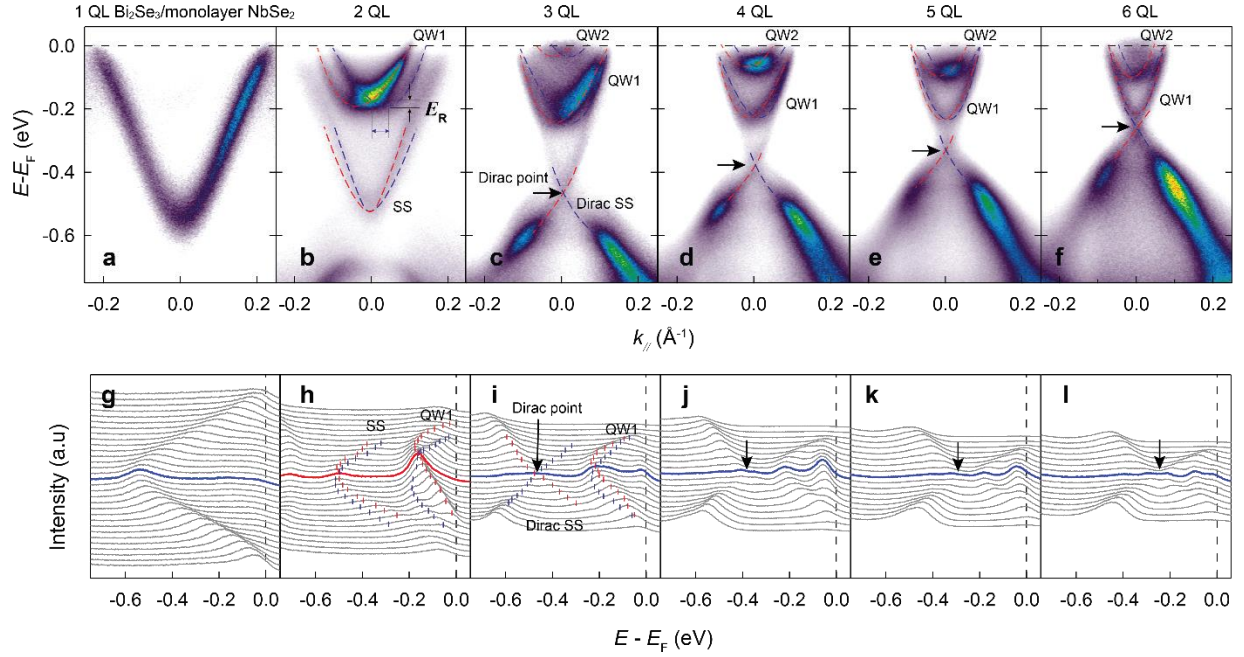


Figure 2 | ARPES band maps of Bi₂Se₃/monolayer NbSe₂ heterostructures. (a-f) ARPES results of m QL Bi₂Se₃/monolayer NbSe₂ heterostructures with $m = 1$ (a), $m = 2$ (b), $m = 3$ (c), $m = 4$ (d), $m = 5$ (e), and $m = 6$ (f). (g-l) The corresponding energy distribution curves (EDCs) of the ARPES results shown in (a-e). The Rashba-type surface states (i.e. SS) and Rashba-type bulk QW states (i.e. QW1 and QW2) are highlighted by the red and blue dashed lines. The ARPES experiments were performed at room temperature. For the Bi₂Se₃ thickness greater than 3 QL, the Dirac point is formed and the second-lowest Rashba-type bulk QW states (i.e. QW2) appear.

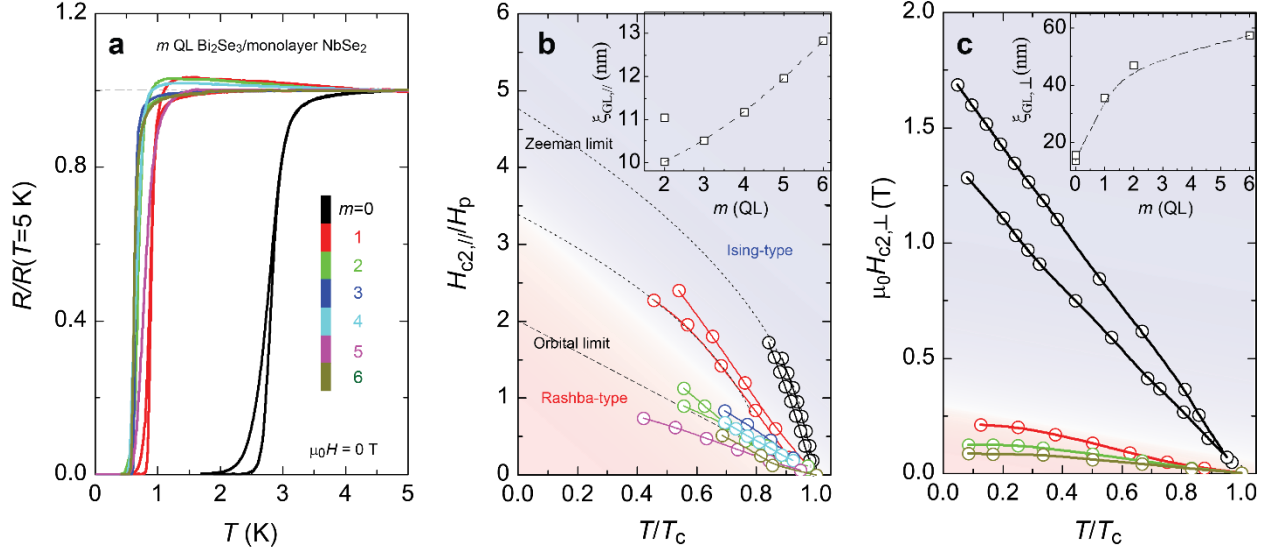


Figure 3 | Crossover of Ising- to Rashba-type pairing symmetry in $\text{Bi}_2\text{Se}_3/\text{monolayer NbSe}_2$ heterostructures. (a) $R - T$ curves of the m QL $\text{Bi}_2\text{Se}_3/\text{monolayer NbSe}_2$ heterostructures under zero magnetic field. R is normalized to the normal state resistance at $T = 5$ K. The superconducting transition temperature T_c is suppressed for $m \geq 1$. The enlarged $R-T$ curves are shown in Fig. S5. (b) The in-plane upper critical magnetic field normalized to the Pauli paramagnetic limit, $H_{c2,\parallel}/H_P$, as a function of the reduced temperature T/T_c for the m QL $\text{Bi}_2\text{Se}_3/\text{monolayer NbSe}_2$ heterostructures. (c) The out-of-plane upper critical magnetic field $H_{c2,\perp}$ as a function of the reduced temperature T/T_c for the m QL $\text{Bi}_2\text{Se}_3/\text{monolayer NbSe}_2$ heterostructures. Insets of (b and c) are the in-plane and out-of-plane Ginzburg-Landau coherence lengths $\xi_{GL,\parallel}$ and $\xi_{GL,\perp}$ as a function of m , respectively. Two $m=0$ samples are included in (a to c). Two $m=1$ and $m=2$ samples are included in (a to b).

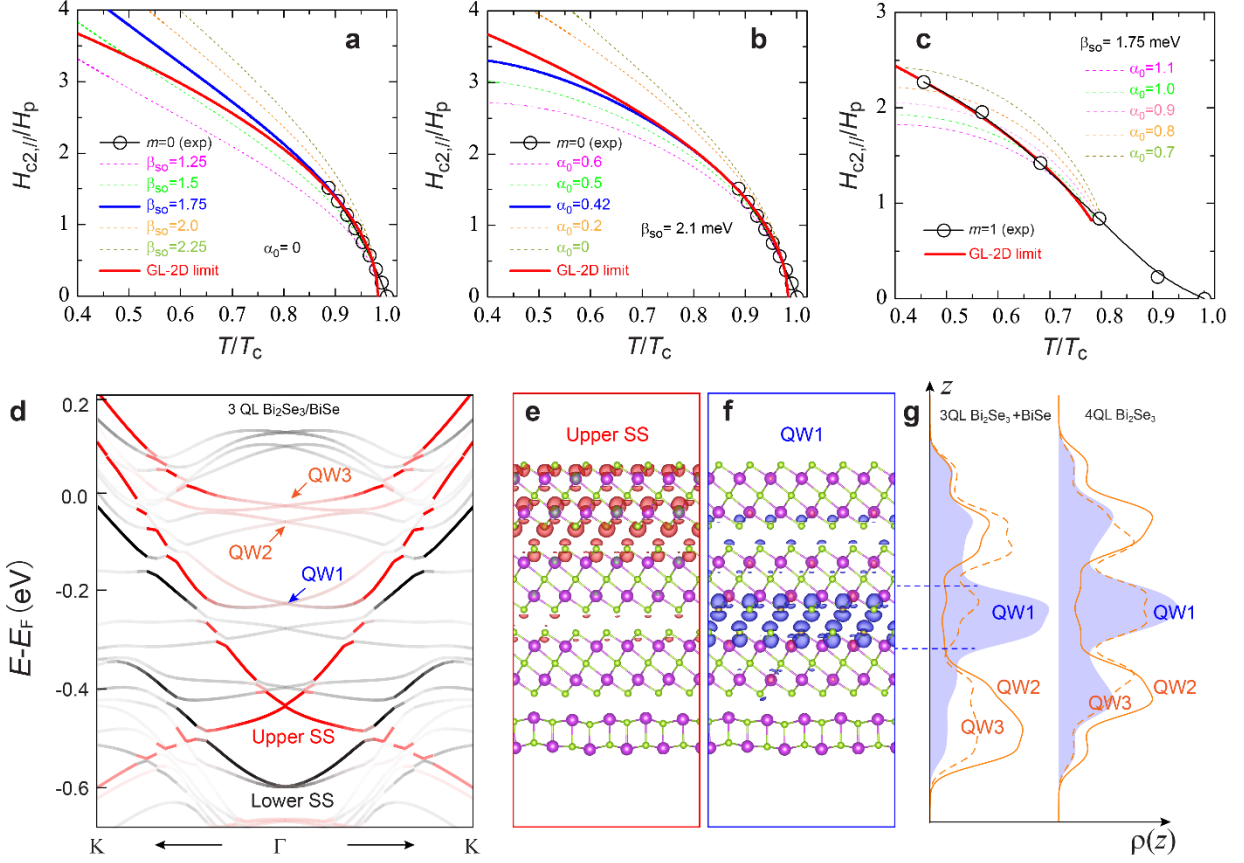


Figure 4 | Theoretical calculations of $\text{Bi}_2\text{Se}_3/\text{monolayer NbSe}_2$ heterostructures. (a to c) The calculated in-plane upper critical magnetic field normalized to the Pauli paramagnetic field $H_{C2,\parallel}/H_P$ as a function of the normalized temperature T/T_C under different Ising-type spin-orbit coupling strength β_{so} and Rashba-type spin-orbit coupling energy α_0 . In (a), for the $m = 0$ sample, we considered β_{so} from 1.25 to 2.25 meV and $\alpha_0 = 0$. The best fit is approached with $\beta_{so} = 1.75$ meV and $\Delta T_C = -0.04$ K (blue solid line) for our experimental data (black circles), consistent with the GL-2D limit fit near T_C (red solid line). In (b), we included a small α_0 from 0 to 0.6 meV with fixed $\beta_{so} = 2.1$ meV for the $m = 0$ sample. The best fit is achieved for a weak $\alpha_0 = 0.42$ meV, indicating that the Ising-type Cooper pairs are still dominant in the $m = 0$ sample. In (c), the experimental data of the $m = 1$ sample can not be fitted by either linear- T behavior (GL-3D limit) or square-root- T behavior (GL-2D limit, red solid line). A moderate fit with two comparable spin-

orbit coupling parameters, i.e., $\alpha_0 \sim 0.9$ meV and $\beta_{so} \sim 1.75$ meV indicates the occurrence of the crossover from 2D Ising-type to 3D bulk Rashba-type superconductivity in the $m = 1$ sample. (d) The calculated band structure of 3QL Bi₂Se₃/BiSe heterostructure. The projections of the total wave function onto Bi orbitals on the upper and lower surfaces of 3QL Bi₂Se₃ are shown in red and black. More Rashba-type QW states in bulk conduction bands are marked by arrows. (e, f) Partial charge densities for the upper SS (e) and the first QW state (f). (g) Charge densities averaged in xy -plane plotted along z , for the three QW states in 3 QL Bi₂Se₃/BiSe heterostructure and the three QW states in a freestanding 4 QL Bi₂Se₃ film.